Journal of Materials Chemistry B

ROYAL SOCIETY OF CHEMISTRY

PAPER

View Article Online
View Journal | View Issue

Cite this: J. Mater. Chem. B, 2024, 12, 2054

Silver oxide decorated urchin-like microporous organic polymer composites as versatile antibacterial organic coating materials†

Yu Zhang,‡*[ad] Yunxin Tang,‡[b] Qian Liao,[b] Yiduo Qian,[a] Linglin Zhu,[c] Deng-Guang Yu,[b] Yixin Xu,[a] Xiuhong Lu,[a] Il Kim*[e] and Wenliang Song*[b]

Received 6th November 2023,
Accepted 22nd January 2024

DOI: 10.1039/d3tb02619a

rsc.li/materials-b

Microporous organic polymers (MOPs) and metal oxide hybrid composites are considered valuable coating materials because of their versatility derived from the synergistic combination of MOPs' inherent dispersibility and the distinctive properties of metal oxides. In this study, we present the synthesis of sea-urchin-like MOPs hybridised with silver oxide nanoparticles (Ag_2O NPs) to fabricate antibacterial composites suitable for potential antibacterial coating applications. Ag_2O NP-decorated urchin-like MOPs (Ag_2O@UMOPs) were synthesised by employing a combination of two methods: a one-pot Lewis acid–base interaction-mediated self-assembly and a straightforward impregnation process. The as-prepared Ag_2O@UMOPs demonstrated high antibacterial efficacy against both *E. coli* (G−) and *S. aureus* (G+). The antibacterial mechanism of Ag_2O@UMOPs mainly involved the synergistic effects of accumulation of Ag_2O@UMOPs, the release of Ag^+ ions, and the generation of reactive oxygen species. The exceptional processability and biosafety of Ag_2O@UMOPs make them ideal organic coating materials for convenient application on various substrates. These remarkable features of Ag_2O@UMOPs provide an effective platform for potential antibacterial applications in biological sciences.

Introduction

Bacterial infections pose a significant threat to public health worldwide as they can lead to severe diseases. Clinically, bacterial infections are typically characterised by chills, high fever, rash, arthralgia, and hepatosplenomegaly.[1,2] Some patients may present with infectious shock and migratory lesions. Pathogenic microorganisms commonly invade the bloodstream through wounds or infected lesions and cause acute systemic infections. Therefore, there is an urgent need to develop effective antibacterial coating materials to minimise the risk of wound infections.[3–6] These coating materials also facilitate the treatment of bacterial contaminants in various environments.[7–9] In recent years, metallic oxide materials (*e.g.* Ag_2O, ZnO, MgO, CaO, CoO, TiO_2, Cu_2O, TiO_2, and Fe_xO_y) have garnered attention owing to their bacteriostatic and/or bactericidal effect.[10,11] Metal ions such as Ca^{2+}, Mg^{2+}, Cu^{2+}, Zn^{2+}, and Co^{2+} play essential roles in various metabolic processes in living bacterial strains and typically become toxic only at higher concentrations.[12] Interestingly, non-essential metal ions, such as Hg^{2+} and Ag^+, present much stronger antibacterial activity, even at low concentrations.[13–15] Because of their detrimental environmental impact, Hg^{2+} ions are not suitable candidates for obtaining antibacterial materials.[16,17] Consequently, Ag^+ ions were more suitable for this purpose. Silver oxide nanoparticles (Ag_2O NPs) demonstrate superior antibacterial activity because of the continuous release of Ag^+ ions. These ions can easily destroy bacterial cell walls by binding to oppositely charged components of the bacterial membrane.[18,19] On the other hand, Ag_2O NPs can generate reactive oxygen species (ROS) such as hydrogen peroxide (H_2O_2), superoxide ($^{\bullet}O_2^-$), and hydroxyl ($^{\bullet}OH$) radicals, which can induce oxidative stress and disrupt bacterial membranes.[20]

Ag_2O NPs are commonly prepared by physical and chemical methods. Physical methods such as microwave, ball milling, laser, and quenching can yield Ag_2O NPs with high purity. However, they often require expensive machinery and involve

[a] Shanghai Key Laboratory of Molecular Imaging, School of Pharmacy, Shanghai University of Medicine and Health Sciences, Shanghai 201318, P. R. China. E-mail: zhangy_21@sumhs.edu.cn
[b] School of Materials and Chemistry, University of Shanghai for Science and Technology, Shanghai 200093, P. R. China. E-mail: wenliang@usst.edu.cn
[c] Department of Oncology, Huadong Hospital Affiliated to Fudan University, No. 139 Yan An Xi Road, Shanghai, 200040, P. R. China
[d] State Key Laboratory of Molecular Engineering of Polymers, Fudan University, Shanghai 200433, P. R. China
[e] School of Chemical Engineering, Pusan National University, Busan 46241, Republic of Korea. E-mail: ilkim@pusan.ac.kr

† Electronic supplementary information (ESI) available. See DOI: https://doi.org/10.1039/d3tb02619a

‡ These authors contributed equally to this work.

harsh conditions.[21,22] Chemical methods involving mixing a silver precursor with ammonia can easily produce Ag_2O NPs.[23,24] However, the agglomeration of particles caused by their high surface energy significantly hampers their practical applications. It should be mentioned that particle size, shape, and surface properties are crucial factors in determining their antibacterial performance.[25–27] Polymer stabilisers, surfactants, and solid supports are commonly used to reduce particle agglomeration.[28] Although numerous reports are available on the preparation and characterisation of polymer-stabilised silver, methods for preparing polymer-stabilised silver oxide are scarce. In addition, Ag_2O NPs have been reported to show low toxicity to soil microorganisms, while displaying high toxicity to pathogenic microorganisms. This property significantly enhances the antibacterial selectivity for specific antibacterial applications. Accordingly, there is a significant demand for the development of stable and effective platforms to address bacterial infections.[29–31]

Microporous organic polymers (MOPs) and metal oxide hybrid materials with advanced coating properties have been proven valuable for a variety of applications.[32–35] Because of their extremely high surface areas, hierarchical pore channels, and versatile surface modification abilities, MOPs have the inherent strength to support Ag_2O NPs.[36,37] MOPs feature abundant micro-, meso-, and macropores, which can be readily controlled to achieve hierarchical pore size distributions. The cross-linked frameworks, combined with the hierarchical pore sizes, created numerous transportation channels that were well suited for the deposition of Ag_2O NPs. MOPs typically exhibit well-defined and controlled morphologies. With respect to the hollow urchin-like morphologies, Ag_2O NPs have the capability to decorate both surfaces of the frameworks and be anchored inside the holes, thereby significantly reducing the possibility of agglomeration. In addition, MOPs with surface carboxyl functionalities can interact with Ag^+ ions under basic conditions, ensuring successful hybridisation as composites for specific coating applications. Although a number of studies have investigated the antimicrobial effect of MOPs loaded with Ag, few have investigated the antimicrobial effect of Ag_2O on MOPs, and it is urgent to investigate the compound antimicrobial effect and mechanism.

Hyper-crosslinked polymers (HCPs) are useful MOP materials commonly obtained with high stability and porosity under mild reaction conditions.[38–41] Recently, we developed a unique Lewis acid–base interaction-mediated self-assembly method that allowed the *in situ* formation of hollow spherical HCPs with hydroxyl functionality.[42,43] Specifically, the one-pot Friedel–Crafts self-crosslinking reaction using 1,4-benzenedimethanol as the monomer and iron chloride as the catalyst enabled the formation of HCPs characterised by inner hollow structures and outer needle-shaped spheres, resembling sea urchins. These sea-urchin-like HCPs spontaneously formed under suitable conditions without the use of templates. We envision that these HCP-based MOPs with defined morphologies and functionalities can serve as ideal supports for Ag_2O NPs.

Herein, we report the synthesis and characterisation of Ag_2O NP-decorated urchin-like MOPs (Ag_2O@UMOPs) as versatile antibacterial coatings (Fig. 1). Ag_2O NPs were anchored onto sea urchin-like MOPs by applying a combination of Lewis acid–base interaction-mediated self-assembly and a straightforward impregnation process. The UMOP scaffolds were first synthesised using a one-pot Friedel–Crafts alkylation reaction. UMOPs contain an abundance of carboxyl groups originating from residual hydroxyl groups that undergo carboxylation through a reaction with chloroacetic acid, greatly facilitating the exchange process with Ag^+ ions. Successful anchoring of highly dispersed Ag_2O NPs into UMOPs was achieved *via* an *in situ*

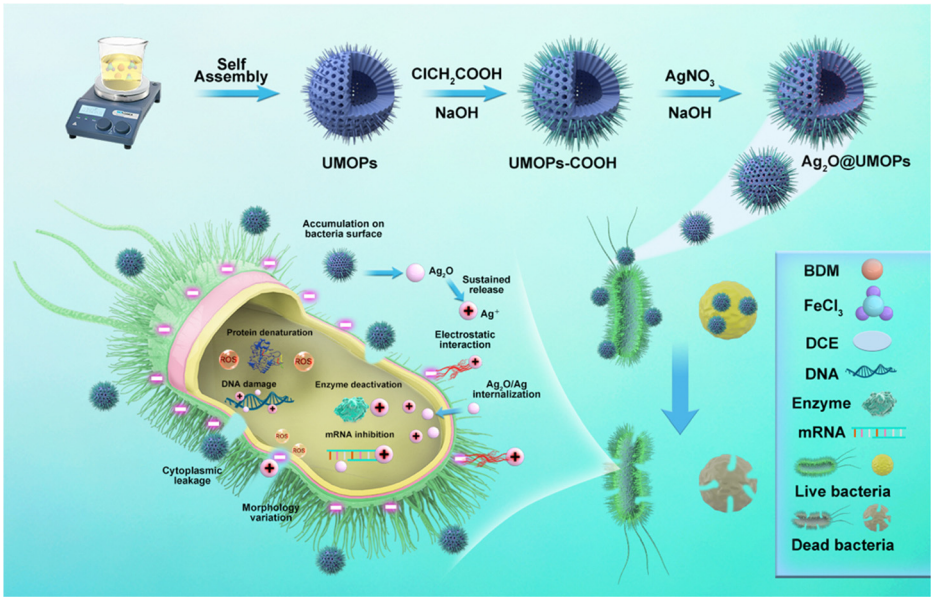

Fig. 1 Schematic diagram of the preparation and antibacterial application of Ag_2O@UMOPs.

reduction process employing NaOH, leading to the formation of Ag_2O@UMOPs. The resultant Ag_2O@UMOPs exhibited outstanding antibacterial activity against both Gram-negative bacteria (*E. coli*) and Gram-positive bacteria (*S. aureus*). Specifically, at a concentration of 200 μg mL^{-1}, Ag_2O-3@UMOPs exhibited antibacterial efficiencies of 99.80% for *E. coli* and 95.30% for *S. aureus*. More importantly, the Ag_2O@UMOPs can be easily loaded into polyurethane foam or compressed into a membrane, demonstrating their superior processability. Furthermore, Ag_2O@UMOPs also showed good biocompatibility and hemocompatibility. The Ag_2O@UMOPs show great advantages of distinctive sea-urchin-like morphologies, a stable crosslinked structure, high surface area, and abundant micro/mesopores, which may offer sufficient transfer channels for bacteria-containing solutions to contact the active sites on the composites. These features render Ag_2O@UMOPs suitable for coating various substrates to meet various biomedical application requirements.

Experimental

Materials

1,4-Benzenedimethanol, chloroacetic acid, 1,2-dichloroethane, acetone, and ethanol were purchased from TCI Chemicals. Anhydrous $FeCl_3$ (98%), $AgNO_3$, NaOH, concentrated HCl and ammonia were obtained from Merck. The solvents used for the reactions were dried over CaH_2, fractionally distilled, and then degassed. The ultrapure water (18.2 MΩ cm^{-1}) used in the experiment was obtained from Milli-Q apparatus. Filter papers, nonwoven fabrics, and PET foam were obtained from a local market.

Preparation of Ag_2O@UMOPs

Ag_2O@UMOPs were prepared according to the following protocol: UMOPs were synthesised through a one-pot Lewis acid–base interaction-mediated self-assembly process, as extensively documented in our prior study.[42,43] Briefly, the 1,4-benzenedimethanol (1 mol, 0.65 g) was mixed with $FeCl_3$ (2 mol, 1.54 g) in the dry 1,2-dichloroethane solutions under a N_2 atmosphere, subsequently, the temperature was set as 80 °C to let the reaction happen. After 18 h, the resultant turbid mixture was filtered and the obtained brown product was sequentially rinsed with acetone, ethanol, and deionised water until the filtrate became clear. The crude solids collected were extracted using ethanol through a Soxhlet process and then dried under vacuum at 80 °C (yield: 112%, based on hypothetical 100% condensation).

The abundant hydroxyl groups present in the UMOPs underwent facile conversion to carboxyl groups through a reaction with chloroacetic acid.[44,45] Briefly, the as-prepared UMOPs (0.30 g) were mixed with 150 mL of deionised water *via* a process involving both stirring and sonication to yield a well-dispersed solution. Chloroacetic acid (15.00 g) and NaOH (18.00 g) were added to the solution for a comprehensive reaction. The reaction mixture was suspended in a dilute HCl solution. The collected crude solids were thoroughly washed with deionised water and dried to yield carboxyl group-terminated UMOPs (UMOPs-COOH, yield: 58%).

UMOPs-COOH (0.10 g) was dispersed in a 6 mol L^{-1} NaOH solution and stirred for 10 h. The salinised carboxyl group-terminated UMOPs and $AgNO_3$ (0.01 g) were introduced in 50 mL alkaline aqueous solution and allowed to stir at 70 °C for 12 h. The crude solids were separated by centrifugation and washed several times with an excess of deionised water and absolute ethanol to remove physically adsorbed Ag species from the UMOPs. The final products were dried under vacuum at 50 °C for 24 h. By changing the weight ratio of $AgNO_3$ to UMOPs (0.10, 0.20, and 0.30), the resulting products, named Ag_2O-1@UMOPs, Ag_2O-2@UMOPs, and Ag_2O-3@UMOPs, were successfully synthesised.

Characterization

Fourier-transform infrared (FT-IR) spectroscopy was performed on a Shimadzu IRPrestige-21 spectrophotometer using the conventional KBr method. The X-ray diffraction (XRD) patterns were observed using a Bruker D8 ADVANCE powder diffractometer using Cu-K_α irradiation (λ = 0.154 nm). The angle-resolved X-ray photoelectron spectroscopy (AR-XPS) analysis was performed on the Theta Probe angle-resolved system using monochromatic Al-K_α X-ray radiation at 1486.6 eV. A Quantachrome Instruments Nova 3200e operator (USA) was used for N_2 adsorption/desorption isotherm analysis. Under a flowing N_2 atmosphere, the thermogravimetric analysis (TGA, Scinco N-1000) was conducted with a heating rate of 10 °C min^{-1} in the temperature range of 30 °C to 800 °C. Differential scanning calorimetry (DSC) analysis was performed on the TA Q200 instrument at a heating rate of 10 °C min^{-1} under a N_2 atmosphere. The morphologies of the UMOPs and Ag_2O@UMOPs were characterised using field-emission scanning electron microscopy (SEM, Zeiss Supra 25) and transmission electron microscopy (TEM, H-7600 HITACHI). The fine inner shapes and compositions of the Ag_2O@UMOPs were observed using a high-resolution transmission electron microscope (HR-TEM, TALOS F200X) equipped with a high-angle annular dark-field-scanning transmission electron microscope (HAADF-STEM) and an energy-dispersive X-ray (EDX) spectrometer.

Antibacterial analysis

The antibacterial properties of different materials were evaluated using *E. coli* and *S. aureus* as representative bacterial models. To ensure full contact, bacterial suspensions (1×10^6 CFU mL^{-1}) were separately incubated with UMOPs and Ag_2O@UMOPs at concentrations of 25, 50, 100 and 200 μg mL^{-1}, maintaining the incubation at 37 °C for 12 h. 100 μL of co-culture was subjected to serial dilution in phosphate buffered saline (PBS). 10 μL of the diluted co-cultures was dispersed onto blood agar plates and inoculated at 37 °C for 24 h. Finally, the surviving colonies of bacteria were counted. A positive control group was established using PBS instead of the polymer. The bacterial growth curves of the different materials were measured using the optical density method. Different

concentrations of UMOPs and Ag_2O@UMOPs were individually incubated with bacterial suspensions (1×10^6 CFU mL^{-1}) at 37 °C for 12 h. The optical density at 600 nm (OD_{600}) was measured for each co-culture at intervals of 2 h. All experiments were conducted in triplicate.

Bacterial membrane integrity test

The integrity of the bacterial cell membrane was assessed using SEM analysis and a live/dead Baclight staining assay. A bacterial suspension was cultivated with 200 μg mL^{-1} Ag_2O@UMOPs at 37 °C for 12 h. Bacterial suspensions without Ag_2O@UMOPs were used as the control group. To observe the morphologies, the bacteria were subjected to centrifugation and PBS washing, followed by fixation in a 2.50% solution of glutaraldehyde and paraformaldehyde at 4 °C for 4 h. Afterward, the fixed bacteria were transferred to sliding cards and dehydrated at the gradient concentration of ethanol solution for 15 min. The surface morphology of the dried bacteria was examined using SEM. The LIVE/DEAD® BacLight™ Bacterial Viability and Counting Kit reagents were used to stain the bacteria. Both the control and Ag_2O@UMOP-treated groups were incubated with propidium iodide (PI) and SYTO9 dyes in a dark environment at 37 °C for 20 min. The resulting suspension was centrifuged and the cells were resuspended in PBS. Fluorescence analysis was performed using a confocal laser fluorescence microscope (CLSM ZEISS 800).

The release behaviour of Ag^+ ions

Ag_2O@UMOPs were immersed in 20 mL of PBS solution (pH = 7.4) at 37 °C. At different intervals (2, 4, 8, 12, 24, and 48 h), determined volumes of the suspensions were removed and centrifuged. The resulting supernatants were filtered through a 0.22 μm membrane and subsequently analysed to determine the concentrations of Ag^+ ions using inductively coupled plasma mass spectroscopy (ICP-MS, Agilent 7500, Agilent, America).

Intracellular ROS level assay

E. coli and *S. aureus* were stained with ROS-sensitive dye DCFH-DA for 20 min at 37 °C in the dark. The bacterial suspensions were incubated with Ag_2O@UMOPs at concentrations of 25, 50, 100 and 200 μg mL^{-1} for 4 h. The resulting bacterial suspensions were collected, centrifuged, and resuspended in PBS. The fluorescence intensity was subsequently measured using a microplate reader at an excitation/emission wavelength of 488/525 nm. H_2O_2 served as the positive control for ROS generation, whereas untreated bacteria served as the negative control.

In vitro cytotoxicity test

To assess the cytotoxicity of the prepared polymers, the MTT assay was performed on mouse embryonic fibroblast cells (NIH-3T3). NIH-3T3 cells were treated with different concentrations of polymers in 96-well microtitre plates and incubated at 37 °C for 24 h. Then, 100 μL of the MTT solution was added into each well and co-cultured for another 4 h. 200 μL of DMSO was added into each well to thoroughly dissolve the purple formazan crystals. Absorbance was recorded using a microplate reader. Untreated bacterial cells served as controls.

Hemolysis assay

The hemolytic activities of the as-prepared polymers were evaluated using fresh mouse blood samples. Briefly, red blood cells were separated by centrifugation and diluted in PBS. The diluted red blood cells were incubated with different concentrations of polymers at 37 °C for 4 h. Each mixture was subjected to centrifugation, and the absorbance of the resulting supernatant was quantified using a UV-vis spectrophotometer. Deionised water was used as the positive control, whereas PBS was used as the negative control.

Results and discussion

Synthesis and characterization of Ag_2O@UMOPs

The overall synthesis procedure for Ag_2O@UMOPs is shown in Fig. 1. In a precisely controlled experiment, the synthesis of the UMOPs involved a mixture of 1,4-benzenedimethanol and $FeCl_3$ in a 1,2-dichloroethane solution. Initially, the hydroxyl groups of 1,4-benzenedimethanol are activated through interactions with a Lewis acid ($FeCl_3$), resulting in the formation of hydroxyl methyl-substituted intermediates. The reaction exhibited rapid progress, evident as dark brown precipitates forming within just 3 min at 80 °C. This indicates a near-simultaneous incidence of alkylation, polymerisation, and self-intercrosslinking in the solution state. Subsequently, the reactions were allowed to proceed for an additional 24 h to ensure thorough crosslinking. Following filtration, washing, Soxhlet extraction, and vacuum drying, the resulting materials (denoted as UMOPs) were characterised as fine powders with chrome yellow hues. Our lab has effectively illustrated that imperfect Friedel–Crafts cross-linking reactions can endow HCPs with *in situ* hydroxyl functionality.[42] Moreover, our earlier research demonstrated the substantial advantages conferred by hydroxyl groups in enabling the incorporation of a diverse array of chemistries.[46–48] Consequently, the carboxylation reaction involving chloroacetic acid under basic conditions successfully transformed the branched hydroxyl groups on the UMOP surface into carboxyl groups, leading to the production of UMOPs with carboxyl-terminated functionalities (UMOPs-COOH). Then, UMOPs-COOH was subjected to salinisation under basic conditions to facilitate exchange with Ag^+ ions *via* electrostatic interactions.[49,50] Subsequently, the successful anchoring of highly dispersed Ag_2O NPs into the UMOPs was achieved *via* an *in situ* reduction process using NaOH, resulting in the formation of Ag_2O@UMOPs.

SEM and TEM were used to observe variations in both the surface and internal morphologies of the UMOPs before and after decoration with Ag_2O NPs. The SEM images reveal the globular morphology of the UMOPs, while simultaneously showing numerous rod-like structures on the surface of the spheres, resembling the spiny sea urchin (Fig. 2(a1)). The TEM

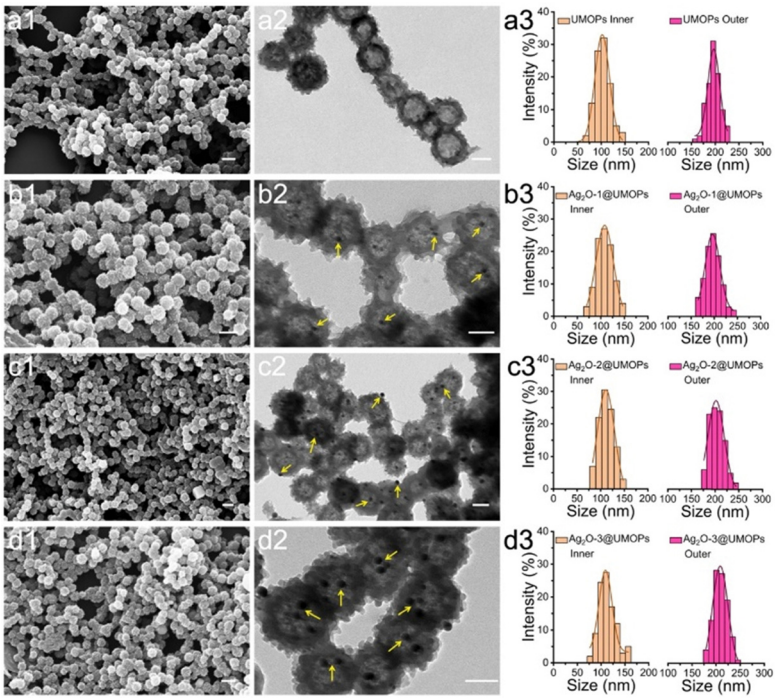

Fig. 2 SEM images of (a1) UMOPs, (b1) Ag_2O-1@UMOPs, (c1) Ag_2O-2@UMOPs, and (d1) Ag_2O-3@UMOPs. Scale bars: 300 nm. TEM images of (a2) UMOPs, (b2) Ag_2O-1@UMOPs, (c2) Ag_2O-2@UMOPs, and (d2) Ag_2O-3@UMOPs. Scale bars: 100 nm. Size distribution diagrams of the interior and exterior diameters of (a3) UMOPs, (b3) Ag_2O-1@UMOPs, (c3) Ag_2O-2@UMOPs, and (d3) Ag_2O-3@UMOPs.

images clearly reveal a well-defined boundary at the edge of the sphere, indicating the inherent hollow morphology of the UMOPs (Fig. 2(a2)). The particle size distribution exhibited a distinct Gaussian distribution pattern (Fig. 2(a3)). The spheres had an outer diameter of 189 nm and an inner diameter of 106 nm, and the rods were between 20 and 29 nm in diameter. Following surface modification with carboxyl groups, sea-urchin-like morphologies were preserved, with only a small portion of the rods displaying slight blunting (Fig. S1, ESI†). After further decoration with Ag_2O NPs, the SEM images of Ag_2O@UMOPs displayed the retained sea-urchin-like morphologies (Fig. 2(b1)–(d1)). Furthermore, a smoother surface was observed compared with the initial protruding surface of the UMOPs. The TEM images of the Ag_2O@UMOPs clearly revealed the existence of Ag_2O NPs, both within the interior and on the surface of the UMOPs (Fig. 2(b2)–(d2)). Gradually increasing the $AgNO_3$ to UMOPs weight ratio from 0.10 to 0.30 resulted in a noticeable increase in the average size of the Ag_2O NPs, advancing from 12.41 to 20.50 nm (Fig. S2, ESI†). Additionally, the particle size distributions of the Ag_2O@UMOPs continued to display a Gaussian distribution pattern, with a slight increase in the outer diameter to approximately 200 nm (Fig. 2(b3)–(d3)).

HR-TEM analysis was carried out to characterize the crystalline structure of Ag_2O@UMOPs. Fig. 3(a1) and (a2) clearly reveal the distribution of the crystalline Ag_2O NPs within the amorphous UMOP matrix. The lattice fringe of 0.27 nm can be indexed to the (111) plane of crystalline Ag_2O (Fig. 3(a3)).[51,52] EDX mapping images illustrate the coexistence of Ag with C and O, providing additional evidence of the successful anchoring of Ag_2O NPs within the entire UMOP framework (Fig. 3(b1)–(b5), (c), and Fig. S3, ESI†). Remarkably, these highly dispersed Ag_2O NPs, whether situated on the surface or embedded within the interior of the UMOPs, provided numerous active sites conducive to engaging with and killing bacteria effectively.

FT-IR spectroscopy and XRD measurements were conducted to further characterise the chemical composition of the Ag_2O@UMOPs. As shown in Fig. S4 (ESI†), the cross-linked polymer skeleton of UMOPs exhibits distinct characteristic bands, including the C–H bending vibration band around 1436 cm^{-1}, the aromatic C=C stretching vibration band around 1630 cm^{-1}, C–H stretching vibration band around 2850 cm^{-1}, aromatic C–H stretching vibration band around 2920 cm^{-1}, and O–H stretching vibration band around 3440 cm^{-1}. The new bands that appeared at approximately 1740 cm^{-1}, 1218 cm^{-1}, and 919 cm^{-1} are assigned to the C=O, C–O, and O–H stretching vibrations of carboxyl groups, respectively;[53,54] they suggest that carboxyl groups were successfully conjugated onto the surfaces of UMOPs. However, the characteristic peaks associated with the carboxyl groups nearly vanished upon decoration with Ag_2O NPs. This may be attributed to the decarboxylation of UMOP-COOH under alkaline conditions.[55,56] In Fig. 4(a), the wide-angle XRD profile of the UMOPs features a broad diffraction peak, consistent with earlier research findings, indicating the inherent amorphous nature of UMOPs.[42,43] Upon the formation of Ag_2O@UMOPs, new diffraction peaks appearing at 2θ values approximately 32.20, 38.30, 54.80, 67.50, and 77.80 correspond to the (111),

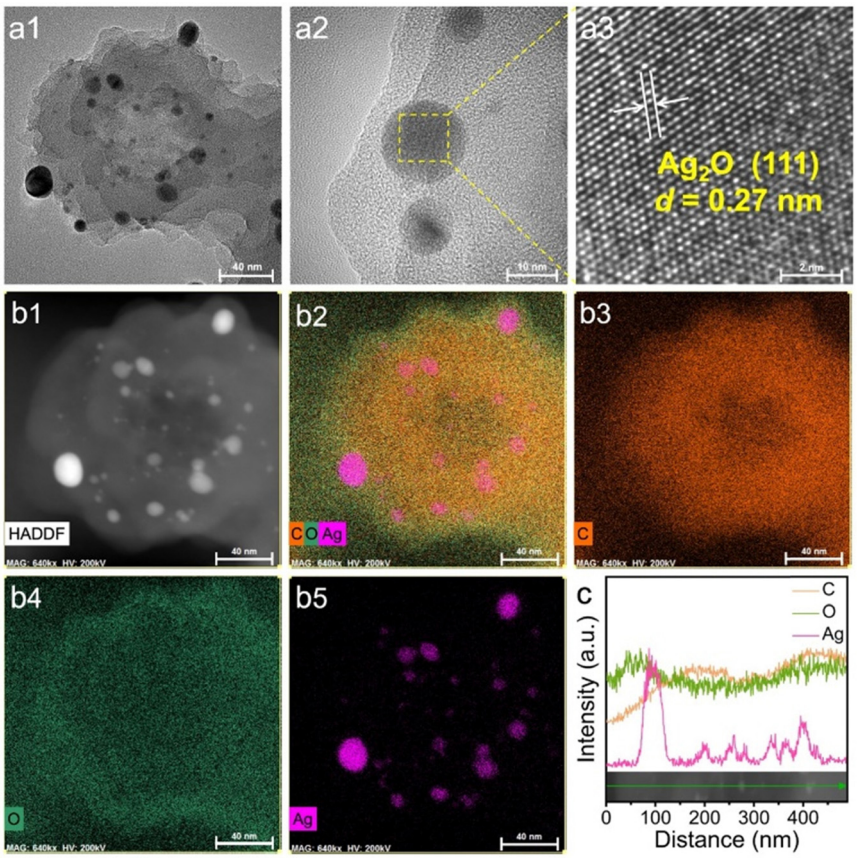

Fig. 3 HR-TEM (a1)–(a3), HAADF-STEM (b1), and EDX mapping (b2)–(b5) images, and energy dispersive spectroscopy line scan of Ag_2O@UMOPs. Scale bars: 40 nm in a1 and b1–b5, 10 nm in a2, and 2 nm in a3.

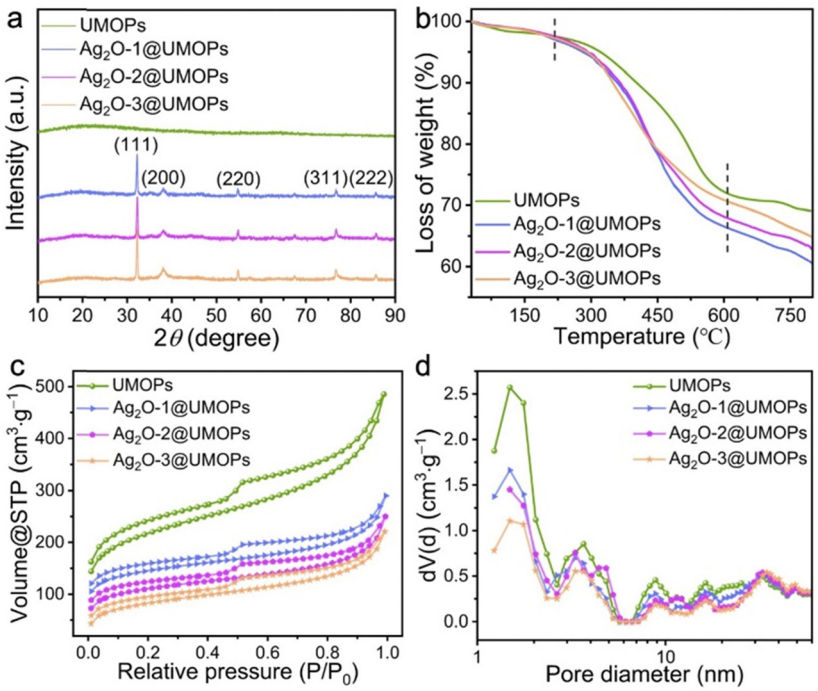

Fig. 4 (a) XRD patterns, (b) TGA curves, (c) N_2 adsorption–desorption isotherms, and (d) NL-DFT pore–size distribution curves.

(200), (220), (311), and (222) crystal faces of Ag_2O, respectively.[57–59] The diffraction peaks of Ag (0) were not observed. By employing the Scherrer equation, the average crystallite sizes of Ag_2O NPs were calculated to be 12.93, 15.74, and 22.31 nm for Ag_2O-1@UMOPs, Ag_2O-2@UMOPs, and Ag_2O-3@UMOPs, respectively. These characteristic peaks collectively offer compelling proof of the crystalline nature of the Ag_2O NPs within the amorphous UMOP framework, which agrees with the findings of the HR-TEM analysis.

To assess the thermal stability of the as-prepared Ag_2O@UMOPs, TGA measurements were carried out under a flowing N_2 atmosphere, covering a temperature range from 25 to 800 °C. As depicted in Fig. 4(b), the negligible weight loss observed in all samples below 120 °C can be attributed to the removal of interstitial water and gas molecules. A dramatic weight decrease occurred in the temperature range of 330–580 °C, which is related to the decomposition of the polymeric framework. As documented in previous studies, the decomposition of Ag_2O NPs occurs at temperatures above 300 °C.[60,61] This factor could be responsible for the faster decomposition of Ag_2O@UMOPs compared to the UMOPs. Above 600 °C, the weight loss curve of UMOPs showed a gentle trend, while the weight of Ag_2O@UMOPs continued to decrease because of the progressive liberation of O_2 absorbed by the polymeric framework. Therefore, the residual weight of Ag_2O@UMOPs was lower than that of UMOPs. The residual weights of the UMOPs, Ag_2O-1@UMOPs, Ag_2O-2@UMOPs, and Ag_2O-3@UMOPs were calculated to be 69.15%, 60.64%, 62.97%, and 65.03%, respectively. It can be observed that the weight loss of Ag_2O@UMOPs decreases as the weight ratio of $AgNO_3$ to UMOPs increases from 0.10 to 0.30 because of the increased content of residual Ag after decomposition.[62] The high thermal stability of the Ag_2O@UMOPs plays a crucial role in their applicability for antibacterial applications, particularly because many antibacterial polymeric counterparts are limited by their inferior thermal stability.

The unique structures of porous networks endow them with high porosity and a large surface area, thereby offering significant advantages for the effective decoration and transportation of specific guest molecules.[42,63,64] N_2 adsorption–desorption analysis was conducted to evaluate variations in the porosity and surface area of the Ag_2O@UMOPs. Fig. 4(c) and (d) display the corresponding pore-size distributions, calculated using nonlocal density functional theory (NL-DFT). All samples exhibited typical IV characteristics, confirming the coexistence of hierarchical micro-, meso-, and macropores. As shown in Table 1, the Brunauer–Emmett–Teller (BET) surface areas were calculated as 967.03, 551.26, 486.09, and 413.75 $m^2\ g^{-1}$ for UMOPs, Ag_2O-1@UMOPs, Ag_2O-2@UMOPs, and Ag_2O-3@UMOPs, respectively. Significantly, the specific surface areas exhibited a gradual decrease upon doping with Ag_2O NPs, accompanied by the corresponding reductions in the pore volume and pore diameter. This can be explained by the abundant embedding of Ag_2O NPs within the UMOP pores, which causes them to occupy a partial portion of the pore volume, resulting in a decrease in the surface area. Compared

Table 1 Yield and textural properties of UMOPs and Ag_2O@UMOPs

Entry	Samples	S_{BET}[a] ($m^2\ g^{-1}$)	V_t[b] (cc g^{-1})	D_p[c] (nm)
1	UMOPs	967.03	0.95	6.24
2	Ag_2O-1@ UMOPs	551.26	0.77	6.18
3	Ag_2O-2@ UMOPs	486.09	0.64	6.09
4	Ag_2O-3@ UMOPs	413.75	0.61	6.03

[a] BET surface areas obtained from the N_2 adsorption isotherms. [b] Total pore volume (P/P_0 = 0.99). [c] Average pore diameter.

to other silver-based scaffolds such as poly(L-lactide), cellulose, chitosan, and poly(*N*-isopropyl acrylamide), Ag_2O@UMOPs provide a considerably large surface area and an abundance of hierarchical pore channels.[65–67] Ag_2O NPs could situate on the surface or embed within the interior of the UMOPs, and this provides numerous active sites to engaging with and killing bacteria. These attributes significantly facilitated the adsorption of bacteria-containing solutions, enabling direct and intimate interactions between the bacteria and the active sites of Ag_2O@UMOPs. Moreover, the surface area of Ag_2O@UMOPs surpasses even that of porous polymer-derived silver nanocomposites, such as metal–organic frameworks, mesoporous silica nanoparticles, and imidazole-based porous organic polymers (Table S1, ESI†). Collectively, the large surface areas and the abundant hierarchical pores significantly facilitated the adsorption of bacteria-containing solutions, enabling direct and intimate interactions between the bacteria and the active sites of Ag_2O@UMOPs.

XPS analysis provided further insights into the detailed surface components of all the polymers, as well as the exact oxidation states of the elements. The UMOPs exhibit two main peaks at approximately 285 and 532 eV, corresponding to C 1s and O 1s, respectively (Fig. 5(a) and Table S2, ESI†). As illustrated in Fig. 5(b), the C 1s deconvoluted peaks at 284.60, 285.50, and 289.70 eV corresponded to the C–C/C=C, C–O, and C=O bonds, respectively. The deconvoluted O 1s peaks at 532.20, 532.71, and 533.42 eV corresponded to the C=O and C–O bonds, as well as adsorbed O, respectively (Fig. 5(c)). In addition, Ag_2O@UMOPs displayed two additional peaks at 367.71 and 373.80 eV, which can be attributed to Ag $3d_{5/2}$ and Ag $3d_{3/2}$, respectively (Fig. 5(d)). These peaks are in agreement with XPS data previously reported for the Ag^+ state.[68,69] Additionally, the deconvoluted O 1s peak at 530.11 eV, attributed to the O–Ag bond, further confirmed the successful decoration of the Ag_2O NPs (Fig. 5(c)).[70] These findings are in good agreement with the XRD results. The Ag_2O NP content within Ag_2O-1@UMOPs, Ag_2O-2@UMOPs, and Ag_2O-3@UMOPs was estimated to be 3.83, 6.59, and 7.54%, respectively.

Antibacterial properties of Ag_2O@UMOPs

E. coli (Gram-negative bacteria) and *S. aureus* (Gram-positive bacteria) were used as representative model bacteria to investigate the antibacterial activity of the synthesised polymers. As shown in Fig. 6(a) and (b), all polymers exhibited concentration-dependent antibacterial ability; the higher the concentration, the better the antibacterial performance. The

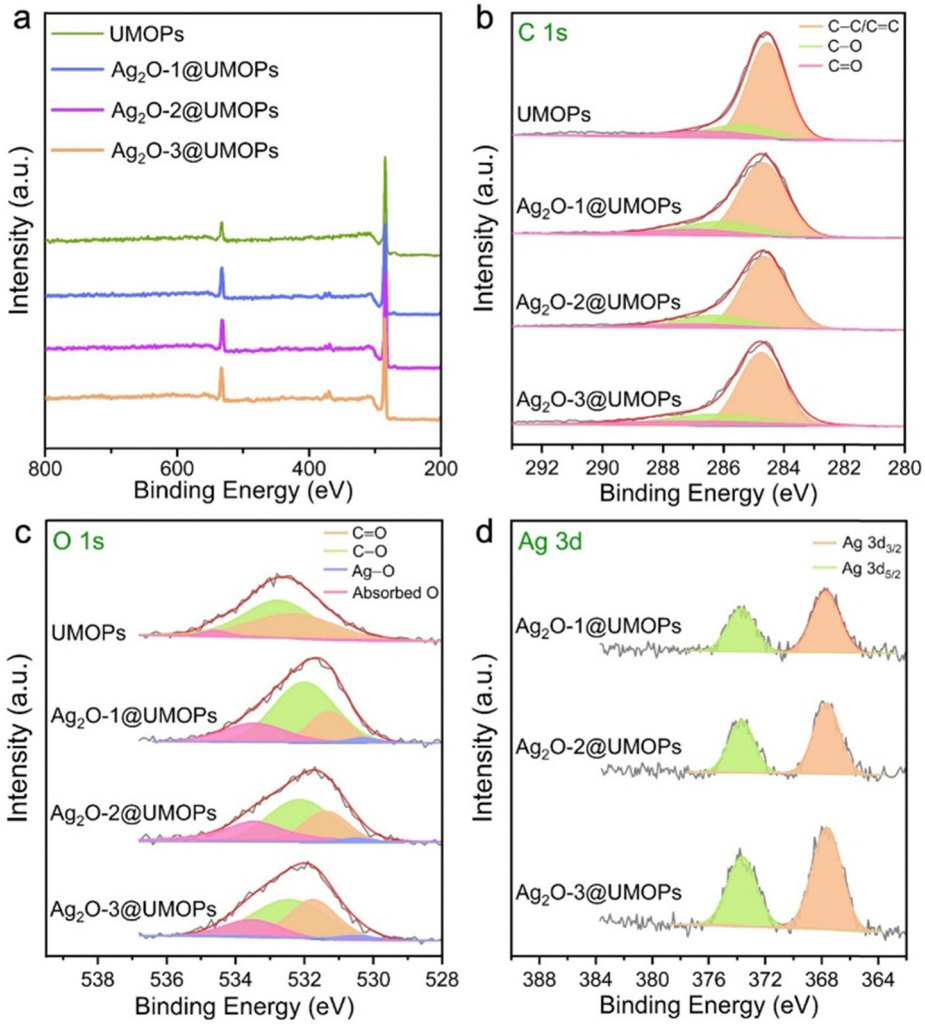

Fig. 5 (a) XPS survey profiles, and deconvoluted XPS profiles for (b) C 1s, (c) O 1s, and (d) Ag 3d of UMOPs, Ag_2O-1@UMOPs, Ag_2O-2@UMOPs and Ag_2O-3@UMOPs.

UMOPs had an almost negligible impact on *E. coli* and *S. aureus* viability, whereas all Ag_2O@UMOPs demonstrated a significant antibacterial effect. This could be attributed to the destructive effects of the Ag_2O NPs embedded in the UMOPs. When *E. coli* were treated with 100 μg mL^{-1} of Ag_2O-1@UMOPs, Ag_2O-2@UMOPs, and Ag_2O-3@UMOPs, the antibacterial efficiencies were about 64.53%, 82.40%, and 88.22%, respectively. Furthermore, as the concentration increased to 200 μg mL^{-1}, the corresponding killing efficiencies of Ag_2O-1@UMOPs, Ag_2O-2@UMOPs, and Ag_2O-3@UMOPs reached 91.62%, 95.57%, and 99.80%, respectively. With regard to *S. aureus*, the killing efficiencies of Ag_2O-1@UMOPs, Ag_2O-2@UMOPs, and Ag_2O-3@UMOPs at a concentration of 100 μg mL^{-1} were 58.28%, 75.85%, and 81.50%, respectively. When the concentration was elevated to 200 μg mL^{-1}, the corresponding antibacterial efficiencies increased to 78.71%, 90.29%, and 95.30%, respectively. Remarkably, the Ag_2O-3@UMOPs groups demonstrated the best antibacterial performance, probably owing to the highest loading content of Ag_2O NPs.

A bacterial growth kinetic curve assay was performed to further investigate the antibacterial properties of the synthesised polymers. *E. coli* and *S. aureus* were incubated with the UMOPs and Ag_2O@UMOP solutions at different concentrations. The growth curves of both *E. coli* and *S. aureus* displayed a significant time-dependent trends (Fig. 6(c), (d) and Fig. S5, S6, ESI†). A macroscopic bacterial proliferation phenomenon was observed for UMOP-treated groups, implying that UMOPs had an almost negligible ability to eradicate bacteria, even at a high concentration of 4 mg mL^{-1}. As the concentration increased to 8 mg mL^{-1}, UMOPs presented a certain inhibitory effect on the growth of both *E. coli* and *S. aureus*, probably owing to the membrane stress exerted on bacterial cell walls by the sharp edges and rough surfaces of UMOPs.[48,71,72] Compared to UMOPs, 200 μg mL^{-1} of Ag_2O@UMOPs considerably inhibited the growth of *E. coli* and *S. aureus* within the initial 6 h. Thereafter, OD_{600} values of Ag_2O-1@UMOPs and Ag_2O-2@UMOPs groups gradually increased after incubating for 8 h, suggesting that neither group was able to completely kill

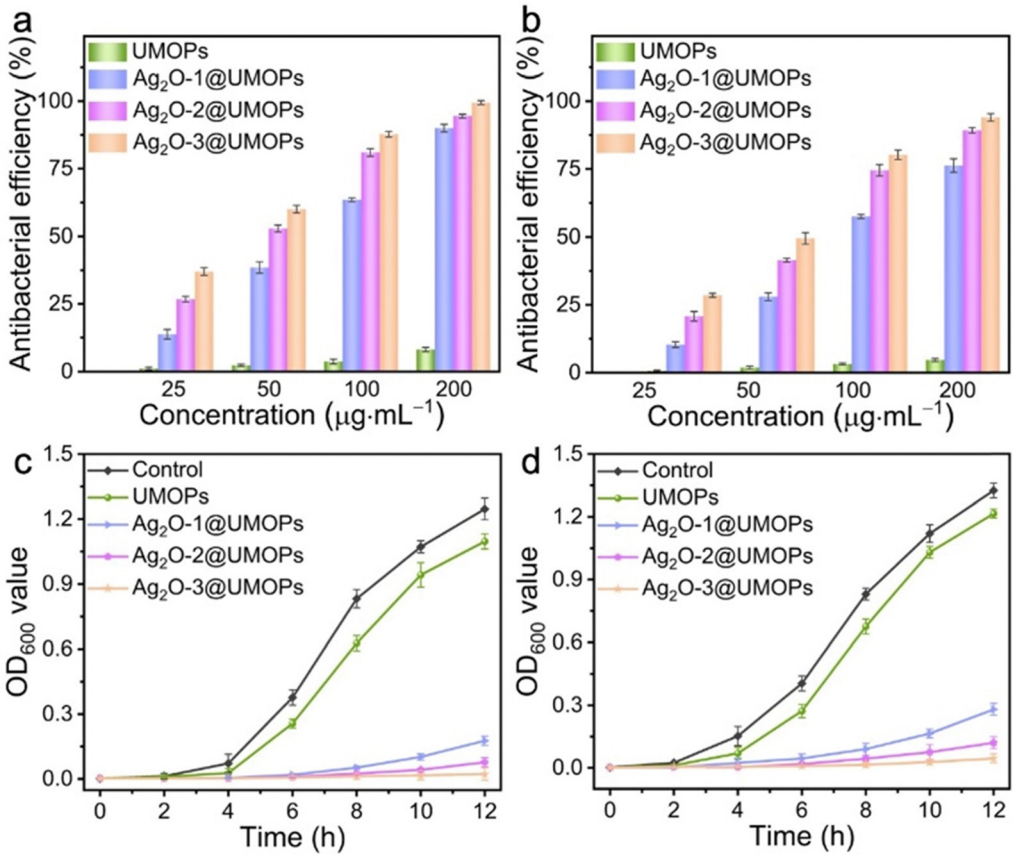

Fig. 6 Antimicrobial activity of UMOPs and Ag_2O@UMOPs against (a) *E. coli* and (b) *S. aureus*. Growth curves of (c) *E. coli* and (d) *S. aureus* treated with UMOPs and Ag_2O@UMOPs (200 μg mL^{-1}), respectively.

bacteria. Nonetheless, the growth curves of the groups treated with 200 μg mL^{-1} of Ag_2O-3@UMOPs exhibited an almost flat trend, indicating that the bacteriostatic effect of Ag_2O-3@UMOPs is better than those of Ag_2O-1@UMOPs and Ag_2O-2@UMOPs. Compared to the most reported composites incorporating Ag or Ag_2O NPs, Ag_2O-3@UMOPs exhibited outstanding antibacterial performance, even with a low Ag_2O NP content of only 7.54% (Table S1, ESI†). Remarkably, the antibacterial efficacy against *E. coli* was notably superior to that against *S. aureus*, likely because of the thicker peptidoglycan layer in the cell walls of *S. aureus*.[73] Measurements were conducted to compare the antimicrobial activity of Ag_2O@UMOPs with that of pure Ag_2O NPs. It should be noted that the antimicrobial activity of pure Ag_2O NPs reached approximately 100% only at a concentration of 100 μg mL^{-1} (Fig. S7, ESI†). However, the Ag_2O NP content of Ag_2O-3@UMOPs was significantly lower compared to that of pure Ag_2O NPs. This could be attributed to the specific sea urchin-like morphology and the abundance of micro/mesopores in Ag_2O-3@UMOPs.

Antibacterial mechanism of Ag_2O@UMOPs

To elucidate the antibacterial mechanism of Ag_2O@UMOPs, SEM analysis was performed to visually assess the integrity of the bacterial cell membranes. As illustrated in Fig. 7(a1) and (a2), the control groups of *E. coli* and *S. aureus* retained smooth surfaces and the original cellular morphologies. In contrast, the membranes of both *E. coli* and *S. aureus* were severely damaged after treatment with Ag_2O@UMOPs (Fig. 7(a3) and (a4)). The bacterial membranes underwent significant distortion and wrinkling with numerous grooves and pits on their surfaces. Some bacteria showed structural collapse and intracellular component leakage, as evidenced by the presence of pores and severely lysed cell membranes (yellow arrowheads). These findings revealed that Ag_2O@UMOPs can effectively disrupt bacterial cell membranes. The live/dead Baclight staining assay was further conducted to demonstrate the integrity of the bacterial cell membrane.[74] SYTO-9 can stain live bacterial cells and generate green fluorescence, whereas PI can only traverse damaged cell membranes, bind DNA, and emit red fluorescence. As shown in Fig. 7(b1) and (b3), the control groups exhibited strong green fluorescence and negligible red fluorescence, suggesting the integrity of the bacterial cell membrane. In contrast, the Ag_2O@UMOP-treated groups displayed prominent red fluorescence, indicating substantial cell membrane damage in the bacteria (Fig. 7(b2), (b4) and Fig. S8, ESI†). The combined results from the SEM images and staining assays confirmed that Ag_2O@UMOPs disturbed membrane permeability and caused significant morphological changes in bacterial cell membranes. This cascade of effects ultimately leads to the destruction of cell membranes and, consequently, the death of

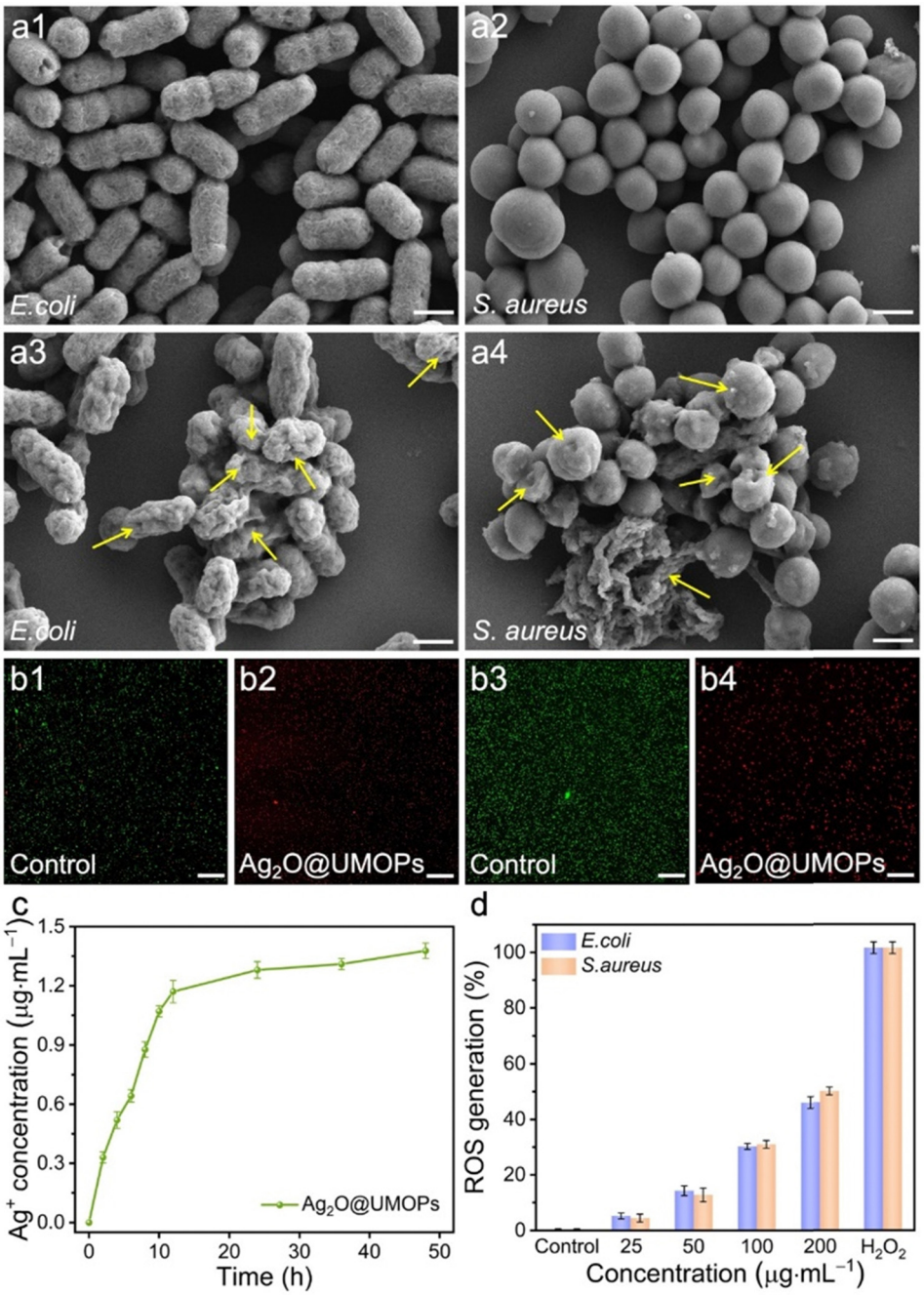

Fig. 7 SEM images of control and Ag_2O@UMOP-treated groups of (a1), (a3) *E. coli* and (a2), (a4) *S. aureus*. Scale bars: 500 nm. (b) Confocal fluorescence microscopy images of control and Ag_2O@UMOP-treated groups of (b1), (b3) *E. coli* and (b2), (b4) *S. aureus*. Scale bars: 200 μm. (c) Cumulative Ag^+ release profile of Ag_2O@UMOPs (200 μg mL^{-1}) in PBS (pH 7.4). (d) Concentration-dependent ROS generation of *E. coli* and *S. aureus* treated with Ag_2O@UMOPs.

the bacteria. It is well-established that Ag_2O NPs can release Ag^+ ions and ROS through the dissolution of environmental O_2 or in response to an acidic environment (primarily induced by the metabolic behaviour of bacteria).[75] Moreover, Ag^+ ions can interact with sulfur- and phosphorus-containing membrane proteins that are abundant on the surface of bacteria.[20,21] Hence, we speculate that Ag^+ ions released from Ag_2O NPs act on the bacterial cell membrane through electrostatic interactions, resulting in enhanced membrane permeability and subsequent membrane disruption. The release of Ag^+ ions from Ag_2O@UMOPs was monitored at different time intervals. Fig. 7(c) clearly illustrates the initial rapid release of Ag^+ ions followed by a steady release after immersion for 12 h. Ag_2O anchored into the hierarchical network of UMOPs enabled the sustained release of Ag^+ ions for more than 50 h, a duration sufficient for effective bacterial

elimination. Additionally, the bacterial cell environment may promote the release of Ag^+ ions owing to the electrostatic interaction between Ag^+ ions and negatively charged groups on membrane proteins.[76]

Previous studies have demonstrated that metal ions and metal-based NPs can promote the generation of ROS such as hydrogen peroxide (H_2O_2), superoxide ($^{\bullet}O^{2-}$), and hydroxyl radicals ($^{\bullet}OH$) during the metabolic processes of bacteria.[77,78]

The elevation of ROS levels can perturb intracellular activities by interacting with lipids, proteins, and DNA, ultimately leading to irreversible oxidative stress. DCFH-DA was selected as the ROS-sensitive probe to evaluate the ROS generation efficiency. DCFH-DA is hydrolysed by intracellular esterases, converting it into non-fluorescent DCFH, which is subsequently oxidised by ROS to produce a green fluorescent product, DCF. Fig. 7(d) illustrates the changes in intracellular ROS levels in both *E. coli* and *S. aureus* when incubated with different concentrations of Ag_2O@UMOPs. Compared to the control group, higher ROS levels were observed in bacteria incubated with different concentrations of Ag_2O@UMOPs. Additionally, there was an increase in the ROS content corresponding to an increase in the concentration of Ag_2O@UMOPs. These findings suggest the generation of a substantial amount of ROS in bacteria when Ag_2O@UMOPs are present, potentially contributing to combating the bacteria.

To gain a profound understanding of the antibacterial mechanism and nanocomposite size within the intricate milieu of Ag_2O@UMOPs, we conducted an investigation into the swelling characteristics of UMOPs, Ag_2O@UMOPs and Ag_2O NPs in complex media, including PBS and LB broth, the designated media for antibacterial activity studies.[42] As depicted in Fig. S9a and b (ESI†), each category of Ag_2O@UMOPs exhibited noticeable swelling after exposure to the solvents for several hours, particularly notable in the case of PBS. The swelling ability (Q) of Ag_2O@UMOPs was quantified by dividing the volume of the swollen polymer by the mass of Ag_2O@UMOPs. Remarkably, Ag_2O@UMOPs demonstrated superior swelling ability, achieving the highest Q value at approximately 40 mL g^{-1} (Fig. S9c, ESI†). Consequently, we postulate that the micro- and mesopore sizes could expand during the swollen state, significantly enhancing the accessible antibacterial sites for interaction with bacteria.[47,48] In contrast, pure Ag_2O NPs did not exhibit a pronounced swelling ability, further validating the advantages of employing such a carrier.

Based on the analysis presented above, we speculate that the bactericidal effect of Ag_2O@UMOPs may be attributed to the synergistic functions of Ag_2O@UMOPs accumulation, release of Ag^+ ions, and generation of ROS. The large surface areas and hierarchical pores create ample channels for bacterial solutions, allowing easy contact and accumulation of Ag_2O@UMOPs on the bacterial surface. Moreover, environmental O_2 and acidic environments can trigger the sustained release of Ag^+ ions and ROS from Ag_2O@UMOPs. The following actions may occur simultaneously: (i) the internalisation of Ag_2O NPs and Ag^+ ions, along with membrane stress induced by the sharp edges and rough surfaces of UMOPs, disrupts the membrane permeability of bacteria.[71,72] (ii) The electrostatic interactions between the Ag^+ ions and the negatively charged groups present in the membrane components further augment the membrane permeability of the bacteria.[75,79] This leads to morphological alterations and damage to the bacterial membrane, ultimately resulting in pore formation and cytoplasmic leakage. (iii) Upon entering cells, Ag_2O NPs and Ag^+ ions perturb bacterial intracellular processes by disrupting the DNA structure, impeding mRNA replication and transcription, denaturing proteins, and deactivating enzyme functions.[31] (iv) Surging ROS levels exacerbate bacterial dysfunction, ultimately leading to bacterial death.[80] Ag_2O@UMOPs functioned as reservoirs for the gradual release of Ag_2O NPs and Ag^+ ions into the bacteria. These sequential actions collectively inhibit the repair of damaged membranes, thereby preventing the development of bacterial drug resistance.

Processability, coating properties and biosafety

Processability plays a pivotal role in the commercialisation of MOPs, enabling the expansion of their potential applications and enhancing their overall performance.[81,82] Therefore, we tested the potential processability of Ag_2O@UMOPs. As shown in Fig. 8(a1) and (a2), the Ag_2O@UMOP powders were loaded into the polyurethane foam, utilizing polydimethylsiloxane (PDMS) as an adhesive by a simple dipping coating method.[43,48,83]

Optical microscopy images demonstrate the continued integrity of the internal structure of the foam, with no noticeable alterations in the pore sizes (Fig. 8(a3) and (a4)). The Ag_2O@UMOP-loaded polyurethane foam excelled at absorbing bacterial solutions, including those found in sewage and medical devices. Simultaneously, the embedded Ag_2O@UMOPs served as potent antimicrobial agents that effectively eradicated bacteria. Moreover, we tested a polytetrafluoroethylene (PTFE) membrane, and the Ag_2O@UMOPs were easily incorporated on the surface of the PTFE membrane (Fig. 8(b1) and (b2)). Ag_2O@UMOP powders, PTFE powders and the PDMS adhesive were uniformly mixed and then mechanically compressed into membranes. This allows for a wider range of applications, such as in air pollutant sterilisation and filtration and as environmental antimicrobials. In addition to the surfaces of common materials, Ag_2O@UMOPs powders can be easily incorporated into PS and further compressed into membranes. As the quantity of Ag_2O@UMOPs increased, a consistent darkening of the heart-shaped membrane colour was clearly observed (Fig. 8(c1) and (c2)). This observation further confirms the exceptional processability of these antibacterial materials. Furthermore, given the impressive antibacterial properties of Ag_2O@UMOPs, PS membranes, with Ag_2O@UMOPs uniformly integrated, have the potential to serve as effective dressing materials for bacterial infections.

The MTT assay was performed on mouse NIH3T3 fibroblasts to evaluate the cytotoxicity of Ag_2O@UMOPs. As depicted in Fig. 8(d), when treated with Ag_2O@UMOPs at concentrations of 25, 50, 100, 200, and 400 μg mL^{-1}, the cell survival rates were found to be 97.52%, 96.80%, 95.27%, 92.45%, and 85.79%,

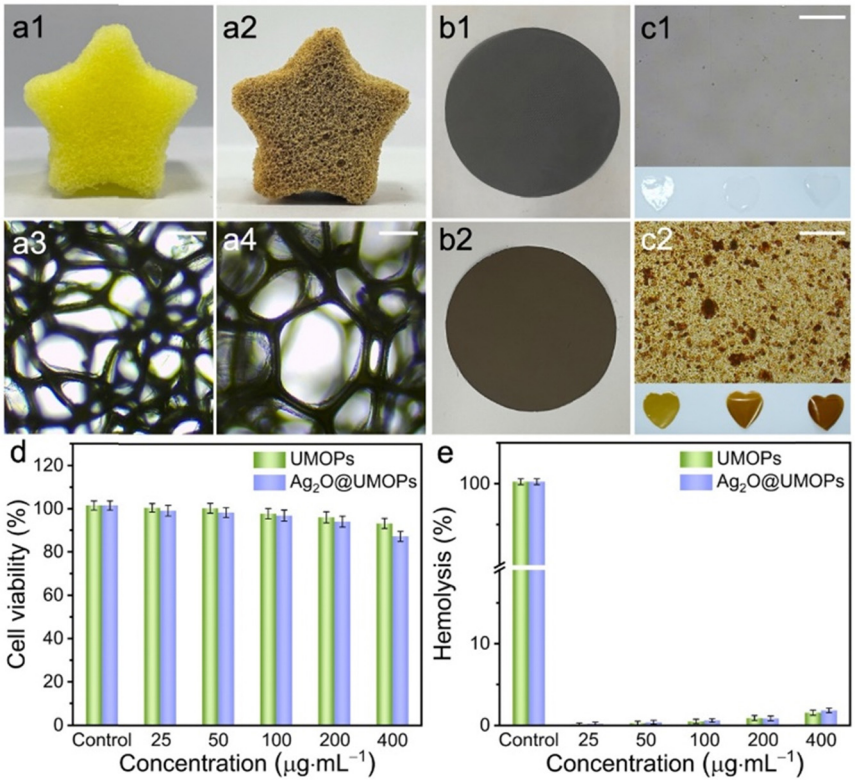

Fig. 8 Photographs of a star-shaped polyurethane foam and the corresponding optical microscopy images of (a1), (a3) before and (a2), (a4) after loading with Ag_2O@UMOPs. Scale bars: 200 μm. Photographs of a PTFE membrane (b1) before and (b2) after loading with Ag_2O@UMOPs. Optical microscopy images of (c1) PS membranes and (c2) PS membranes incorporated with Ag_2O@UMOPs. Scale bars: 100 μm. (d) Cell viability of NIH-3T3 cells after incubation with UMOPs and Ag_2O@UMOPs. (e) Hemolysis assay of UMOPs and Ag_2O@UMOPs.

respectively. In conjunction with the antibacterial results, Ag_2O@UMOPs, at a concentration of approximately 200 μg mL^{-1}, exhibited remarkable capability to eradicate bacteria completely, all while maintaining unaffected cellular activity. A haemolysis assay using fresh mouse blood was conducted to further assess the hemocompatibility of the Ag_2O@UMOPs. Fig. 8(e) shows that no significant haemolytic effect was observed for Ag_2O@UMOPs. These findings indicated the negligible toxicity of Ag_2O@UMOPs at antibacterial concentrations, rendering them an ideal choice for use as organic coating materials on various substrates. These successful attempts also convinced us that these antimicrobial powders can be effectively compounded on the surface or inside a wide range of materials, thus enabling their use in a wider range of applications.

Conclusion

We fabricated a versatile antibacterial coating material based on Ag_2O@UMOPs with a distinctive sea-urchin-like shape. Ag_2O@UMOPs were readily synthesised through a one-pot self-assembly process mediated by Lewis acid–base interactions, followed by carboxylation and anchoring of the Ag_2O NPs. Ag_2O@UMOPs possess a large surface area and high porosity, furnishing a multitude of active sites that are conducive to the effective engagement with and killing of bacteria. The Ag_2O@UMOPs exhibited superior antibacterial activity against both *E. coli* and *S. aureus*. At a concentration of 200 μg mL^{-1}, Ag_2O-3@UMOPs exhibited impressive killing efficiencies of 99.80% for *E. coli* and 95.30% for *S. aureus*. Interestingly, Ag_2O@UMOPs can be easily loaded onto polyurethane foam or compressed into the membrane. Cytotoxicity and haemolysis assays demonstrated good cytocompatibility and hemocompatibility of Ag_2O@UMOPs. Consequently, the remarkable thermal stability, processability, and biosafety of the Ag_2O@UMOPs make them suitable for coating a wide range of substrates to meet various biomedical requirements.

Author contributions

Y. Z. and W. S. conceived the idea and designed the experiments. Y. T., Q. L., and Y. Q. performed the experiments. Y. Z. and Y. X. participated in data analyses and discussions. L. Z., D. G. Y., Y. X., X. L., I. K. and W. S. contributed in writing – reviewing and editing the manuscript.

Conflicts of interest

There are no conflicts to declare.

Acknowledgements

This work was supported by the Shanghai Sailing Program (21YF1431000 and 22YF1417700), Open Research Fund Program of the State Key Laboratory of Molecular Engineering of Polymers (Fudan University, K2023-13), Open Research Fund Program of the Shanghai Key Laboratory of Molecular Imaging (Shanghai University of Medicine and Health Sciences, KFKT-2023-24), and Scientific Research Foundation of the Shanghai University of Medicine and Health Sciences (SSF-22-07-02). IK is thankful for the National Research Foundation of Korea grant funded by the Korean government (MSIT) (2021R1A2C2003685) for financial support.

References

1 J. M. V. Makabenta, A. Nabawy, C.-H. Li, S. Schmidt-Malan, R. Patel and V. M. Rotello, Nanomaterial-based therapeutics for antibiotic-resistant bacterial infections, *Nat. Rev. Microbiol.*, 2021, **19**, 23–36.

2 B. J. Langford, M. So, S. Raybardhan, V. Leung, D. Westwood, D. R. MacFadden, J.-P. R. Soucy and N. Daneman, Bacterial co-infection and secondary infection in patients with COVID-19: a living rapid review and meta-analysis, *Clin. Microbiol. Infect.*, 2020, **26**(12), 1622–1629.

3 Y.-h Wang, Current progress of research on intestinal bacterial translocation, *Microb. Pathog.*, 2021, **152**, 104652.

4 A. Elbourne, S. Cheeseman, P. Atkin, N. P. Truong, N. Syed, A. Zavabeti, M. Mohiuddin, D. Esrafilzadeh, D. Cozzolino and C. F. McConville, *et al.*, Antibacterial liquid metals: Biofilm treatment *via* magnetic activation, *ACS Nano*, 2020, **14**(1), 802–817.

5 T. Li, P. Wang, W. Guo, X. Huang, X. Tian, G. Wu, B. Xu, F. Li, C. Yan and X.-J. Liang, *et al.*, Natural berberine-based chinese herb medicine assembled nanostructures with modified antibacterial application, *ACS Nano*, 2019, **13**(6), 6770–6781.

6 J. Qian, Q. Dong, K. Chun, D. Zhu, X. Zhang, Y. Mao, J. N. Culver, S. Tai, J. R. German and D. P. Dean, Highly stable, antiviral, antibacterial cotton textiles *via* molecular engineering, *Nat. Nanotechnol.*, 2022, 1–9.

7 Z. Sadat, F. Farrokhi-Hajiabad, F. Lalebeigi, N. Naderi, M. Ghafori Gorab, R. Ahangari Cohan, R. Eivazzadeh-Keihan and A. Maleki, A comprehensive review on the applications of carbon-based nanostructures in wound healing: from antibacterial aspects to cell growth stimulation, *Biomater. Sci.*, 2022, **10**(24), 6911–6938.

8 L. Yang, C. Wang, L. Li, F. Zhu, X. Ren, Q. Huang, Y. Cheng and Y. Li, Bioinspired Integration of Naturally Occurring Molecules towards Universal and Smart Antibacterial Coatings, *Adv. Funct. Mater.*, 2022, **32**(4), 2108749.

9 Q. Borjihan and A. Dong, Design of nanoengineered antibacterial polymers for biomedical applications, *Biomater. Sci.*, 2020, **8**(24), 6867–6882.

10 V. Stanić and S. B. Tanasković, Antibacterial activity of metal oxide nanoparticles, in *Nanotoxicity*, ed. S. Rajendran, A. Mukherjee, T. A. Nguyen, C. Godugu and R. K. Shukla, Elsevier, 2020, ch. 11, pp. 241–274.

11 E. Albalghiti, L. M. Stabryla, L. M. Gilbertson and J. B. Zimmerman, Towards resolution of antibacterial mechanisms in metal and metal oxide nanomaterials: a meta-analysis of the influence of study design on mechanistic conclusions, *Environ. Sci.: Nano*, 2021, **8**(1), 37–66.

12 K. B. Muchowska, S. J. Varma and J. Moran, Nonenzymatic metabolic reactions and life's origins, *Chem. Rev.*, 2020, **120**(15), 7708–7744.

13 M. Godoy-Gallardo, U. Eckhard, L. M. Delgado, Y. J. de Roo Puente, M. Hoyos-Nogués, F. J. Gil and R. A. Perez, Antibacterial approaches in tissue engineering using metal ions and nanoparticles: From mechanisms to applications, *Bioact. Mater.*, 2021, **6**(12), 4470–4490.

14 A. Saenchoopa, W. Boonta, C. Talodthaisong, O. Srichaiyapol, R. Patramanon and S. Kulchat, Colorimetric detection of Hg(II) by γ-aminobutyric acid–silver nanoparticles in water and the assessment of antibacterial activities, *Spectrochim. Acta, Part A*, 2021, **251**, 119433.

15 L. Eskandari, F. Andalib, A. Fakhri, M. K. Jabarabadi, B. Pham and V. K. Gupta, Facile colorimetric detection of Hg(II), photocatalytic and antibacterial efficiency based on silver-manganese disulfide/polyvinyl alcohol-chitosan nanocomposites, *Int. J. Biol. Macromol.*, 2020, **164**, 4138–4145.

16 S. Rashid, I. A. Shah, R. X. S. Tulcan, W. Rashid and M. Sillanpaa, Contamination, exposure, and health risk assessment of Hg in Pakistan: A review, *Environ. Pollut.*, 2022, **301**, 118995.

17 M. Wen, Q. Wu, G. Li, S. Wang, Z. Li, Y. Tang and T. Liu, Impact of ultra-low emission technology retrofit on the mercury emissions and cross-media transfer in coal-fired power plants, *J. Hazard. Mater.*, 2020, **396**, 122729.

18 C. M. Phan and H. M. Nguyen, Role of capping agent in wet synthesis of nanoparticles, *J. Phys. Chem. A*, 2017, **121**(17), 3213–3219.

19 A. Grigor'eva, I. Saranina, N. Tikunova, A. Safonov, N. Timoshenko, A. Rebrov and E. Ryabchikova, Fine mechanisms of the interaction of silver nanoparticles with the cells of Salmonella typhimurium and Staphylococcus aureus, *Biometals*, 2013, **26**(3), 479–488.

20 Y. Li, W. Zhang, J. Niu and Y. Chen, Mechanism of photogenerated reactive oxygen species and correlation with the antibacterial properties of engineered metal-oxide nanoparticles, *ACS Nano*, 2012, **6**(6), 5164–5173.

21 W. M. Shume, H. A. Murthy and E. A. Zereffa, A review on synthesis and characterization of Ag_2O nanoparticles for photocatalytic applications, *J. Chem.*, 2020, 1–15.

22 S. V. Gudkov, D. A. Serov, M. E. Astashev, A. A. Semenova and A. B. Lisitsyn, Ag_2O nanoparticles as a candidate for antimicrobial compounds of the new generation, *Pharmaceuticals*, 2022, **15**(8), 968.

23 A. A. Rokade, M. P. Patil, S. I. Yoo, W. K. Lee and S. Park, Pure green chemical approach for synthesis of Ag_2O nanoparticles, *Green Chem. Lett. Rev.*, 2016, **9**(4), 216–222.

24 H. Patel and J. Joshi, Green and chemical approach for synthesis of Ag_2O nanoparticles and their antimicrobial activity, *J. Sol-Gel Sci. Technol.*, 2023, **105**(3), 814–826.
25 G. L. Tan, D. Tang, D. Dastan, A. Jafari, Z. Shi, Q. Q. Chu and X. T. Yin, Structures, morphological control, and antibacterial performance of tungsten oxide thin films, *Ceram. Int.*, 2021, **47**(12), 17153–17160.
26 Y. Wang, Y. Yang, Y. Shi, H. Song and C. Yu, Antibiotic-free antibacterial strategies enabled by nanomaterials: progress and perspectives, *Adv. Mater.*, 2020, **32**(18), 1904106.
27 N. Talank, H. Morad, H. Barabadi, F. Mojab, S. Amidi, F. Kobarfard and E. Mostafavi, Bioengineering of green-synthesized silver nanoparticles: *In vitro* physicochemical, antibacterial, biofilm inhibitory, anticoagulant, and antioxidant performance, *Talanta*, 2022, **243**, 123374.
28 H. Zhao, Y. Yang, Y. Chen, J. Li, L. Wang and C. Li, A review of multiple Pickering emulsions: Solid stabilization, preparation, particle effect, and application, *Chem. Eng. Sci.*, 2022, **248**, 117085.
29 Y. Peng, H. Zhou, Y. Wu, Z. Ma, R. Zhang, H. Tu and L. Jiang, A new strategy to construct cellulose-chitosan films supporting $Ag/Ag_2O/ZnO$ heterostructures for high photocatalytic and antibacterial performance, *J. Colloid Interface Sci.*, 2022, **609**, 188–199.
30 J. Zhou, L. Wang, W. Gong, B. Wang, D. G. Yu and Y. Zhu, Integrating Chinese herbs and western medicine for new wound dressings through handheld electrospinning, *Biomedicines*, 2023, **11**(8), 2146.
31 Y. Peng, H. Zhou, Z. Ma, L. Tian, R. Zhang, H. Tu and L. Jiang, *In situ* synthesis of Ag/Ag_2O–cellulose/chitosan nanocomposites *via* adjusting KOH concentration for improved photocatalytic and antibacterial applications, *Int. J. Biol. Macromol.*, 2023, **225**, 185–197.
32 J. Mandal, Y. Fu, A. C. Overvig, M. Jia, K. Sun, N. N. Shi, H. Zhou, X. Xiao, N. Yu and Y. Yang, Hierarchically porous polymer coatings for highly efficient passive daytime radiative cooling, *Science*, 2018, **362**(6412), 315–319.
33 S. Wu, J. Xu, L. Zou, S. Luo, R. Yao, B. Zheng, G. Liang, D. Wu and Y. Li, Long-lasting renewable antibacterial porous polymeric coatings enable titanium biomaterials to prevent and treat peri-implant infection, *Nat. Commun.*, 2021, **12**(1), 3303.
34 J. Choi, Y. J. Lee, D. Park, H. Jeong, S. Shin, H. Yun, J. Lim, J. Han, E. J. Kim, S. S. Jeon, Y. Jung, H. Lee and B. J. Kim, Highly durable fuel cell catalysts using crosslinkable block copolymer-based carbon supports with ultralow Pt loadings, *Energy Environ. Sci.*, 2020, **13**, 4921.
35 Y. J. Lee, H. Kim, E. Lee, J. Lee, S. Shin, H. Yun, E. J. Kim, H. Jung, H. C. Ham, B. J. Kim and H. Lee, Ultra-low Pt loaded porous carbon microparticles with controlled channel structure for high-performance fuel cell catalysts, *Adv. Energy Mater.*, 2021, **11**, 2102970.
36 Z. Yuan, Y. Liu and H. Zhou, Chemical crosslinking enabling ferroelectric polymers for new memory applications, *Innovations Mater.*, 2023, **1**(2), 100025.
37 Y. Chen and Y. Zhao, Harnessing whole tumor cells for tumor immunotherapy, *Innovations Mater.*, 2023, **1**(2), 100018.
38 Y. Gu, S. U. Son, T. Li and B. Tan, Low-cost hypercrosslinked polymers by direct knitting strategy for catalytic applications, *Adv. Funct. Mater.*, 2021, **31**(12), 2008265.
39 W. Song, Y. Zhang, C. H. Tran, H. K. Choi, D. G. Yu and I. P. Kim, Porous organic polymers with defined morphologies: Synthesis, assembly, and emerging applications, *Prog. Polym. Sci.*, 2023, **142**, 101691.
40 Q. Liao, E. J. Kim, Y. Tang, H. Xu, D. Yu, W. Song and B. J. Kim, Rational design of hyper-crosslinked polymers for biomedical applications, *J. Polym. Sci.*, 2023, 20230270.
41 S. Yu and M. Antonietti, Creative and relevant materials innovation, *Innovations Mater.*, 2023, **1**(1), 100002.
42 W. Song, Y. Zhang, A. Varyambath and I. Kim, Guided assembly of well-defined hierarchical nanoporous polymers by Lewis acid–base interactions, *ACS Nano*, 2019, **13**(10), 11753–11769.
43 Y. Zhang, S. Li, Y. Xu, X. Shi, M. Zhang, Y. Huang and I. Kim, Engineering of hollow polymeric nanosphere-supported imidazolium-based ionic liquids with enhanced antimicrobial activities, *Nano Res.*, 2022, **15**(6), 5556–5568.
44 Z. Hu, J. Li, C. Li, S. Zhao, N. Li, Y. Wang, F. Wei, L. Chen and Y. Huang, Folic acid-conjugated graphene-zno nanohybrid for targeting photodynamic therapy under visible light irradiation, *J. Mater. Chem. B*, 2013, **1**, 5003–5013.
45 Y. Tian, G. Liang, T. Fan, J. Shang, S. Shang, Y. Ma and S. Kitagawa, Grafting free carboxylic acid groups onto the pore surface of 3D porous coordination polymers for high proton conductivity, *Chem. Mater.*, 2019, **31**(20), 8494–8503.
46 Y. Ji, H. Zhao, H. Liu, P. Zhao and D.-G. Yu, *Gels*, 2023, **9**, 700.
47 W. Song, Y. Zhang, D. G. Yu, C. H. Tran, M. Wang, A. Varyambath and I. Kim, Efficient synthesis of folate-conjugated hollow polymeric capsules for accurate drug delivery to cancer cells, *Biomacromolecules*, 2020, **22**(2), 732–742.
48 W. Song, M. Zhang, X. Huang, B. Chen, Y. Ding, Y. Zhang and I. Kim, Smart l-borneol-loaded hierarchical hollow polymer nanospheres with antipollution and antibacterial capabilities, *Mater. Today Chem.*, 2022, **26**, 101252.
49 B. Shi, Y. Xu, T. Wang, S. Gao, G. Meng and K. Huang, Ag nanoparticles encapsulated in carboxyl-functionalized hollow microporous organic nanospheres for highly efficient catalysis applications, *Appl. Catal., A*, 2019, **588**, 117276.
50 Y. Wang, L. Liu, Y. Zhu, L. Wang, D. G. Yu and L. Y. Liu, Trilayer core–shell fibers from coaxial electrospinning for a modified release of metronidazole, *Pharmaceutics*, 2023, **15**(11), 2561.
51 Z. Bao, Z. Sun, M. Xiao, H. Chen, L. Tian and J. Wang, Transverse oxidation of gold nanorods assisted by selective end capping of silver oxide, *J. Mater. Chem.*, 2011, **21**(31), 11537–11543.
52 X. Wang, Y. Li, X. Guo and Z. Jin, *In situ* synthesis of Ag/Ag_2O on CeO_2 for boosting electron transfer in

photocatalytic hydrogen production, *J. Phys. Chem. C*, 2022, **126**(31), 13015–13024.

53 F. Xie, C. Huang, F. Wang, L. Huang, R. A. Weiss, J. Leng and Y. Liu, Carboxyl-terminated polybutadiene–poly (styrene-*co*-4-vinylpyridine) supramolecular thermoplastic elastomers and their shape memory behavior, *Macromolecules*, 2016, **49**(19), 7322–7330.

54 Y. Zhang, R. Liu, H. Jin, W. Song, R. Augustine and I. Kim, Straightforward access to linear and cyclic polypeptides, *Commun. Chem.*, 2018, **1**(1), 40.

55 J. Luo, H. Chang, A. A. Bakhtiary Davijani, H. C. Liu, P. H. Wang, R. J. Moon and S. Kumar, Influence of high loading of cellulose nanocrystals in polyacrylonitrile composite films, *Cellulose*, 2017, **24**, 1745–1758.

56 Y. H. Hsueh, W. C. Liaw, J. M. Kuo, C. S. Deng and C. H. Wu, ydrogel film-immobilized Lactobacillus brevis RK03 for γ-aminobutyric acid production, *Int. J. Mol. Sci.*, 2017, **18**(11), 2324.

57 D. Guin, S. V. Manorama, J. N. L. Latha and S. Singh, Photoreduction of silver on bare and colloidal TiO_2 nanoparticles/nanotubes: synthesis, characterization, and tested for antibacterial outcome, *J. Phys. Chem. C*, 2007, **111**(36), 13393–13397.

58 T. Wang, H. Xiao, Y. Gao, J. Xu, Z. Zhang, H. Bian and T. Sun, Ag_2O/TiO_2 hollow microsphere heterostructures with exposed high-energy {001} crystal facets and high photocatalytic activities, *J. Mater. Sci.: Mater. Electron.*, 2020, **31**, 11496–11507.

59 J. Fowsiya and G. Madhumitha, Biomolecules derived from Carissa edulis for the microwave assisted synthesis of Ag_2O nanoparticles: A study against S. incertulas, C. medinalis and S. mauritia, *J. Cluster Sci.*, 2019, **30**, 1243–1252.

60 S. O. T. Tobisawa, Magnetochemical Investigation on Thermal decomposition of silver oxide, *Bull. Chem. Soc. Jpn.*, 1959, **32**(11), 1173–1180.

61 I. Nakamori, H. Nakamura, T. Hayano and S. Kagawa, The thermal decomposition and reduction of silver(I) oxide, *Bull. Chem. Soc. Jpn.*, 1974, **47**(8), 1827–1832.

62 M. Cobos, I. De-La-Pinta, G. Quindós, M. J. Fernández and M. D. Fernández, Graphene oxide–silver nanoparticle nanohybrids: Synthesis, characterization, and antimicrobial properties, *Nanomaterials*, 2020, **10**(2), 376.

63 J. S. M. Lee and A. I. Cooper, Advances in conjugated microporous polymers, *Chem. Rev.*, 2020, **120**(4), 2171–2214.

64 Z. Wang, X. Luo, Z. Song, K. Lu, S. Zhu, Y. Yang and J. Jin, Microporous polymer adsorptive membranes with high processing capacity for molecular separation, *Nat. Commun.*, 2022, **13**(1), 4169.

65 E. Lizundia, I. Armentano, F. Luzi, F. Bertoglio, E. Restivo, L. Visai and D. Puglia, Synergic effect of nanolignin and metal oxide nanoparticles into Poly(L-lactide) bionanocomposites: material properties, antioxidant activity, and antibacterial performance, *ACS Appl. Bio Mater.*, 2020, **3**(8), 5263–5274.

66 Y. Peng, H. Zhou, Y. Wu, Z. Ma, R. Zhang, H. Tu and L. Jiang, A new strategy to construct cellulose-chitosan films supporting $Ag/Ag_2O/ZnO$ heterostructures for high photocatalytic and antibacterial performance, *J. Colloid Interface Sci.*, 2022, **609**, 188–199.

67 H. Ji, S. Zhou, Y. Fu, Y. Wang, J. Mi, T. Lu and C. Lü, Size-controllable preparation and antibacterial mechanism of thermo-responsive copolymer-stabilized silver nanoparticles with high antimicrobial activity, *Mater. Sci. Eng., C*, 2020, **110**, 110735.

68 Z. H. Yang, C. H. Ho and S. Lee, Plasma-induced formation of flower-like Ag_2O nanostructures, *Appl. Surf. Sci.*, 2015, **349**, 609–614.

69 G. Maheshwaran, A. N. Bharathi, M. M. Selvi, M. K. Kumar, R. M. Kumar and S. Sudhahar, Green synthesis of silver oxide nanoparticles using zephyranthes rosea flower extract and evaluation of biological activities, *J. Environ. Chem. Eng.*, 2020, **8**(5), 104137.

70 B. Ajitha, Y. A. K. Reddy and P. S. Reddy, Green synthesis and characterization of silver nanoparticles using Lantana camara leaf extract, *Mater. Sci. Eng., C*, 2015, **49**, 373–381.

71 O. Akhavam and E. Ghaderi, Toxicity of graphene and graphene oxide nanowalls aginst bacteria, *ACS Nano*, 2010, **4**, 5731–5736.

72 S. Liu, T. H. Zeng, M. Hofmann, E. Burcombe, J. Wei, R. Jiang, J. Kong and Y. Chen, Antibacterial activity of graphite, graphite oxide, graphene oxide, and reduced graphene oxide: membrane and oxidative stress, *ACS Nano*, 2011, **5**, 6971.e6980.

73 A. Gupta, S. Mumtaz, C.-H. Li, I. Hussain and V. M. Rotello, Combatting antibioticresistant bacteria using nanomaterials, *Chem. Soc. Rev.*, 2019, **48**(2), 415–427.

74 Q. Zhou, X. Lyu, B. Cao, X. Liu, J. Liu, J. Zhao, M. Zhan and X. Hu, Fast broad-spectrum staining and photodynamic inhibition of pathogenic microorganisms by a water-soluble aggregation-induced emission photosensitizer, *Front. Chem.*, 2021, **9**, 755419.

75 Y. Zhao, J. Xu, Z. Li, T. Fu and S. Jiang, *In vitro* antibacterial properties of $MoO_3/SiO_2/Ag_2O$ nanocomposite coating prepared by double cathode glow discharge technique, *Surf. Coat. Technol.*, 2020, **397**, 125992.

76 X. Li, X. Niu, Y. Chen, K. Yuan, W. He, S. Yang and D. G. Yu, Electrospraying micro-nano structures on chitosan composite coatings for enhanced antibacterial effect, *Prog. Org. Coat.*, 2023, **174**, 107310.

77 C. Wang, W. Zhao, B. Cao, Z. Wang, Q. Zhou, S. Lu, L. Lu, M. Zhan and X. Hu, Biofilm-responsive polymeric nanoparticles with self-adaptive deep penetration for *in vivo* photothermal treatment of implant infection, *Chem. Mater.*, 2020, **32**(18), 7725–7738.

78 A. L. Neal, What can be inferred from bacterium–nanoparticle interactions about the potential consequences of environmental exposure to nanoparticles?, *Ecotoxicology*, 2008, **17**, 362–371.

79 X. Guo, B. Cao, C. Wang, S. Lu and X. Hu, *In vivo* photothermal inhibition of methicillin-resistant Staphylococcus aureus infection by *in situ* templated formulation of pathogen-targeting phototheranostics, *Nanoscale*, 2020, **12**(14), 7651–7659.

80 Z. Song, Y. Wu, H. Wang and H. Han, Synergistic antibacterial effects of curcumin modified silver nanoparticles through ROS-mediated pathways, *Mater. Sci. Eng., C*, 2019, **99**, 255–263.
81 J. Zhou, Y. Dai, J. Fu, C. Yan, D. G. Yu and T. Yi, Dual-Step controlled release of berberine hydrochloride from the trans-scale hybrids of nanofibers and microparticles, *Biomolecules*, 2023, **13**(6), 1011.
82 J. Huang, L. Yu, S. Wang, L. Qi, Z. Lu, L. Chen and C. Chen, An ultrathin nanocellulosic ion redistributor for long-life zinc anode, *Innovations Mater.*, 2023, **1**(2), 100029.
83 F. Wang, F. Ren, D. Ma, P. Mu, H. Wei, C. Xiao and A. Li, Particle and nanofiber shaped conjugated microporous polymers bearing hydantoinsubstitution with high antibacterial activity for water cleanness, *J. Mater. Chem. A*, 2018, **6**, 266–274.